Useful Analytical Formulae for Near-Field Monostatic Radar Cross Section Under the Physical Optics: Far-Field Criterion

Christophe Bourlier, *Member, IEEE*, and Philippe Pouliguen

***Abstract*—Radar cross section (RCS) is usually defined in the far-field zone. In this case, RCS is independent of the range of the radar from the object. However, in several scenarios, like for military applications or measurements led in anechoic chambers, the object is located in the near-field zone. From the physical optics (PO) approximation and from some simplying assumptions, this paper presents useful analytical formulae of the monostatic RCS of canonical shape perfectly-conducting objects at oblique incidence angles. The formulae are then compared with the PO integral, which requires two-fold numerical integrations. Finally, the authors also examine the far-field criterion using the resulting expressions.**

***Index Terms*—Electromagnetic scattering, far field, near field, physical optics (PO), radar cross section (RCS).**

I. Introduction

In a RADAR scenario, the radar cross section (RCS) is a normalized power, which quantifies the electromagnetic scattering properties of an object. It is usually defined in the far-field zone. In this case, the RCS is an intrinsic value of the object under test, totally independent of the radar antenna orientation and of the range of the radar from the target. This property is valid if the radar is far enough from the target so that the incident wave appears as locally planar on the object surface and the scattered wave appears as locally planar at the receiver. Thus, the object is seen as a scattering point by the radar. However, in several applications, like military scenarios or measurements led in anechoic chambers, the object under test can be located in the near-field zone, i.e., below the Fraunhofer limit. For instance, in naval environment as in missile/target end-game scenarios, seekers and radar are almost always located in the near-field zone. As a consequence, below the Fraunhofer limit, the near-field RCS depends on the distance R_0 of the target from the radar, and needs to be evaluated with respect to this parameter. To our knowledge, very few works have been published on this task.

Vogel [1] proposed a physical optics (PO) approximation in the near-field region. The object surface is then approximated by flat sized patches, in such a way, that for each patch, the far-field approximation is applied. Then, the integration over each meshing element is carried out analytically. The reflection from the entire object is calculated by a vectorial summation of each elementary contribution.

More recently, Legault *et al.* [2] implemented such a technique to compute the RCS of vessels in realistic configurations. In both of these works, the near-field RCS is defined as the far-field RCS, by omitting the limit $R_0 \rightarrow \infty$ in the definition of the RCS. To simulate the radar returns of an airborne target from mid-course to end-game, the NcPTD and Npatch codes [3] were developed, based on PO/physical theory of diffraction (PTD) and shooting and bouncing rays methods.

Lee *et al.* [4] and Taylor *et al.* [5] proposed other expressions of the near-field RCS, based on the range variations of the radar equation. Instead of calculating the range of the antennas from the object at an arbitrary point, they consider the range of the antennas from the volume centroid of the object as the near-field range.

Pouliguen *et al.* proposed a method [6] to calculate the near-field RCS, based on the PO and the division of the target surface in sub-surfaces (triangular meshes), in such a way that all the elementary surfaces are located in the far-field zone of the transmitter and the receiver. Also, a new definition of near-field RCS was proposed, using the transmitter generator equivalent voltage rather than the incident electric field on the scatterer. This definition allows one to take into account the non uniform magnitude and phase of the incident field on the scatterer. In addition, as the range tends to infinity, it converges to the RCS classical definition in the far-field zone.

To our knowledge, unlike the far-field region, no simple analytical formulae of the near-field RCS of canonical shape targets such as plates, disks, cylinders, and so on, were published. From an appropriate definition of the RCS in the near-field zone [6] and under the PO approximation, this paper presents useful analytical formulae of the monostatic near-field RCS at oblique incidence angles of canonical shape perfectly-conducting flat objects. The formulae are then compared with the PO approximation, which requires two-fold numerical integrations. In what follows, the edge diffraction phenomenon is neglected. This means that the present model can not be applied for grazing incidence angles. Typically, the incidence angle does not exceed 50–60 degrees. The contribution of the edge diffractions can be added separately by using, for instance, the works of Michaeli [10], [11].

The paper is organized as follows. In Sections II and III, the monostatic RCS are derived for a rectangular plate and a disk, and numerical results are presented to test the validity of the

Manuscript received March 07, 2008. Current version published March 04, 2009.

C. Bourlier is with the Laboratory Institut de Recherche en Electrotechnique et Electronique de Nantes Atlantique (IREENA), Radar Team, Polytech'Nantes, 44306 Nantes Cedex 3, France (e-mail: christophe.bourlier@univ-nantes.fr).

P. Pouliguen is with the Centre d'Electronique de L'Armement (CELAR), CGN Division, 35170 Bruz, France.

Color versions of one or more of the figures in this paper are available online at http://ieeexplore.ieee.org.

Digital Object Identifier 10.1109/TAP.2008.2009717

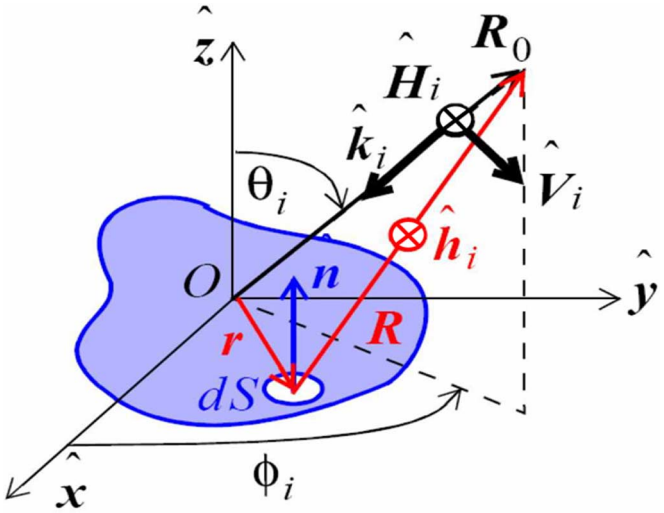

Fig. 1. Description of the problem geometry. The object lies in the (x, y) plane the normal to the surface is $\hat{\mathbf{n}} = \hat{\mathbf{z}}$.

closed-form expressions. In Section IV, the far-field condition is investigated and the last section gives concluding remarks.

II. Near-Field Monostatic RCS

In this paper, the time factor $e^{-j\omega t}$ is assumed. The monostatic RCS in near field, defined from [6], is expressed for a perfectly-conducting object and under the physical optics approximation as

$$\sigma_{e_i e_r}(\theta_i, \phi_i) = \frac{4\pi}{\lambda^2} |f_{e_i e_r}(\theta_i, \phi_i)|^2 \tag{1}$$

where

$$f_{e_i e_r}(\theta_i, \phi_i) = \int\int_S (\hat{\mathbf{R}} \cdot \hat{\mathbf{n}})(\hat{\mathbf{e}}_i \cdot \hat{\mathbf{e}}_r) \frac{R_0^2}{R^2} e^{2jkR} dS. \tag{2}$$

As shown in Fig. 1, R is the distance between a point on the object and the receiver. The vector $\mathbf{r} = (x, y)$ gives the position of a point on the object, assumed to be plane $(z = 0)$. The vector $\mathbf{R}_0 = (R_0 \cos\phi_i \sin\theta_i, R_0 \sin\phi_i \sin\theta_i, R_0 \cos\theta_i)$ gives the position of the receiver defined in polar coordinates from the radial distance $R_0 = ||\mathbf{R}_0||$, the elevation incidence angle (or elevation observation angle) θ_i and the azimuthal incidence angle (or azimuthal observation angle) ϕ_i. The unitary vector $\hat{\mathbf{n}}$ stands for the normal to the surface element $dS = dxdy$ and $\hat{\mathbf{n}} = \hat{\mathbf{z}} \forall (x, y) \in S$. The boldface stands for a vector and the hat $\hat{}$ indicates that the vector is unitary. k is the wave number in the incident medium, assumed to be vacuum.

The incident wave vector is defined as $\hat{\mathbf{k}}_i = -\hat{\mathbf{R}}_0$ and the observation wave vector is defined as $\hat{\mathbf{k}}_r = -\hat{\mathbf{k}}_i$ in the backscattering direction (monostatic case). The vectors $(\hat{\mathbf{e}}_i, \hat{\mathbf{e}}_r)$ stand for the state polarization of the incident and receiver fields, respectively. For the receiver, $\hat{\mathbf{e}}_r = \{\hat{\mathbf{H}}_r, \hat{\mathbf{V}}_r\} = \{\hat{\mathbf{H}}_i, -\hat{\mathbf{V}}_i\}$, and for the emitter, $\hat{\mathbf{e}}_i = \{\hat{\mathbf{h}}_i, \hat{\mathbf{v}}_i\}$, which depends on the vector $\hat{\mathbf{R}}$. Indeed, since in the near-field zone, the vectors $\hat{\mathbf{R}}_0$ and $\hat{\mathbf{R}}$ are not collinear, there is a depolarization effect quantified by the scalar product $\hat{\mathbf{e}}_i \cdot \hat{\mathbf{e}}_r$ in (2).

From Fig. 1, $\mathbf{R} = \mathbf{R}_0 - \mathbf{r} \Rightarrow R = ||\mathbf{R}|| = ||\mathbf{R}_0 - \mathbf{r}||$, leading to

$$\frac{R}{R_0} = \left[1 + \frac{x^2 + y^2}{R_0^2} - 2\sin\theta_i \frac{x\cos\phi_i + y\sin\phi_i}{R_0}\right]^{1/2} \tag{3}$$

and

$$\frac{\hat{\mathbf{R}} \cdot \hat{\mathbf{n}}}{\cos\theta_i} = \left[1 + \frac{x^2 + y^2}{R_0^2} - 2\sin\theta_i \frac{x\cos\phi_i + y\sin\phi_i}{R_0}\right]^{-1/2}. \tag{4}$$

Furthermore, with $\hat{\mathbf{R}} = (\mathbf{R}_0 - \mathbf{r})/||\mathbf{R}_0 - \mathbf{r}||$

$$\begin{cases} \hat{\mathbf{H}}_i = \frac{\hat{\mathbf{k}}_i \wedge \hat{\mathbf{z}}}{||\hat{\mathbf{k}}_i \wedge \hat{\mathbf{z}}||} & \hat{\mathbf{V}}_i = \hat{\mathbf{H}}_i \wedge \hat{\mathbf{k}}_i \\ \hat{\mathbf{h}}_i = \frac{\hat{\mathbf{R}} \wedge \hat{\mathbf{z}}}{||\hat{\mathbf{R}} \wedge \hat{\mathbf{z}}||} & \hat{\mathbf{v}}_i = \hat{\mathbf{h}}_i \wedge \hat{\mathbf{R}} \end{cases}. \tag{5}$$

Thus, from the above expressions, the scalar product $\hat{\mathbf{e}}_i \cdot \hat{\mathbf{e}}_r$ can be derived with respect to (x, y), leading to the calculations of $\hat{\mathbf{h}}_i \cdot \hat{\mathbf{H}}_i, \hat{\mathbf{h}}_i \cdot \hat{\mathbf{V}}_i, -\hat{\mathbf{v}}_i \cdot \hat{\mathbf{H}}_i$ and $-\hat{\mathbf{v}}_i \cdot \hat{\mathbf{V}}_i$, corresponding to the polarizations HH, HV, VH and VV, respectively.

To obtain closed-forms of (2) for canonical-shape objects, like a rectangular plate or a disk, the distance R in the phase term and the factor term $(\hat{\mathbf{R}} \cdot \hat{\mathbf{n}})(R_0^2)/(R^2)$ are approximated by

$$\begin{aligned} R \approx R_0 &- \sin\theta_i (x\cos\phi_i + y\sin\phi_i) \\ &+ \frac{1}{2R_0}\left[x^2(1 - \sin^2\theta_i \cos^2\phi_i)\right. \\ &\left. + y^2(1 - \sin^2\theta_i \sin^2\phi_i) - xy\sin^2\theta_i \sin(2\phi_i)\right] \end{aligned} \tag{6}$$

and

$$(\hat{\mathbf{R}} \cdot \hat{\mathbf{n}})\frac{R_0^2}{R^2} \approx \cos\theta_i \left[1 + \frac{3\sin\theta_i}{R_0}(x\cos\phi_i + y\sin\phi_i)\right] \tag{7}$$

respectively. In (6), a Taylor series expansion was applied on $\{x, y\}$ around $(x, y) = (0, 0)$ up to the orders two, and (7) was obtained from a Taylor series expansion on $\{x, y\}$ around $(x, y) = (0, 0)$ up to the orders one. These expansions are valid if the ratio of the largest dimension of the object to the distance R_0 is small comparatively to unity. In addition, as in (7), using a Taylor series expansion on $\{x, y\}$ around $(x, y) = (0, 0)$ up to the orders one for the scalar product $\hat{\mathbf{e}}_i \cdot \hat{\mathbf{e}}_r$, one can show that

$$\begin{cases} \hat{\mathbf{h}}_i \cdot \hat{\mathbf{H}}_i = -\hat{\mathbf{v}}_i \cdot \hat{\mathbf{V}}_i \approx 1 \\ \hat{\mathbf{h}}_i \cdot \hat{\mathbf{V}}_i = -\hat{\mathbf{v}}_i \cdot \hat{\mathbf{H}}_i \approx \frac{\sin\phi_i \cot\theta_i}{R_0}(y\cos\phi_i - x\sin\phi_i) \end{cases}. \tag{8}$$

Thus, from (1), $\sigma_{VV} = \sigma_{HH}$ and $\sigma_{VH} = \sigma_{HV}$. In what follows, only the VV polarization is investigated and the cross-polarizations are not considered since their contributions are very small comparatively to that of the co-polarizations. In addition, the subscripts $e_i e_r$ in (1) and (2) are omitted.

In [12], the angle $\theta_i = 0$ and only the specific case $\phi_i = \pi/2$ (observation along y) is analyzed. This allows us to simplify (6) and (7) (reduced to $\cos\theta_i$).

III. Case of a Rectangular Plate

A. Derivation of the RCS

In (6), for $\phi_i = \{0, \pi/2\}$, one has $\sin(2\phi_i) = 0$, which allows one to remove the dependence on xy in the phase term e^{2jkR} [see (6) and (2)]. In what follows, this assumption is used.

This permits to separate the double integral (2) over $\{x, y\}$ into two independent integrals over x and y, respectively. Thus, for a rectangular plate of dimensions a (along $\hat{\mathbf{x}}$) and b (along $\hat{\mathbf{y}}$), the substitution of (6) and (7) into (2) yields

$$f(\theta_i,\phi_i) = \cos\theta_i e^{2jkR_0}\left\{ g_0(a,\alpha_c,\beta_c)g_0(b,\alpha_s,\beta_s) + \frac{3\sin\theta_i}{R_0}\left[\cos\phi_i g_1(a,\alpha_c,\beta_c)g_0(b,\alpha_s,\beta_s) + \sin\phi_i g_1(b,\alpha_s,\beta_s)g_0(a,\alpha_c,\beta_c)\right]\right\} \quad (9)$$

where

$$g_0(2a,\alpha,\beta) = \int_{-a}^{+a} e^{j\alpha x^2 - 2j\beta x}dx = \frac{1}{2}\sqrt{\frac{\pi}{-j\alpha}}e^{\frac{-j\beta^2}{\alpha}} \times\left[\operatorname{erf}\left(\frac{\alpha a-\beta}{\sqrt{j\alpha}}\right)+\operatorname{erf}\left(\frac{\alpha a+\beta}{\sqrt{j\alpha}}\right)\right] \quad (10)$$

$$g_1(2a,\alpha,\beta) = \int_{-a}^{+a} xe^{j\alpha x^2 - 2j\beta x}dx = \frac{j}{2}\frac{\partial g_0(2a,\alpha,\beta)}{\partial\beta} = \frac{\beta}{\alpha}\left\{ g_0(2a,\alpha,\beta) + \frac{e^{\frac{-j\beta^2}{\alpha}}}{2j\beta}\left[e^{\frac{j(\alpha x-\beta)^2}{\alpha}}\right]_{x=-a}^{x=+a}\right\} \quad (11)$$

and

$$\begin{cases} \alpha_c = \frac{k}{R_0}(1-c^2) & \alpha_s = \frac{k}{R_0}(1-s^2) \\ \beta_c = kc & \beta_s = ks \\ c = \sin\theta_i\cos\phi_i & s = \sin\theta_i\sin\phi_i \end{cases} \quad (12)$$

Thus, from (10) and (11), f requires the computation of the error function [7] with complex arguments owing to the $(1)/(\sqrt{j})$ term. For this particular case, it is more convenient to use the Fresnel integrals [7] defined from the error function as

$$\operatorname{erf}\left(\frac{x}{\sqrt{j}}\right) = \sqrt{\frac{2}{j}}F\left(x\sqrt{\frac{2}{\pi}}\right) \quad (13)$$

with

$$F(x) = \int_0^x e^{\frac{j\pi t^2}{2}}dt \quad (14)$$

where x is a *real* number since $\{a, b, \beta_c, \beta_s\}$ are real and $\{\alpha_c, \alpha_s\}$ are positive real numbers.

The substitution of (13), (11), (10), and (1) into (9), leads then to

$$\sigma_{\text{plate}}(\theta_i,\phi_i) = \frac{\pi R_0^2\cos^2\theta_i}{4(1-c^2)(1-s^2)}\left| F_{1c}F_{1s} + \frac{3c^2}{1-c^2}F_{1s}(F_{1c}+E_{1c}) + \frac{3s^2}{1-s^2}F_{1c}(F_{1s}+E_{1s})\right|^2 \quad (15)$$

with

$$\begin{cases} F_{1c} = F(u_c+v_c)+F(u_c-v_c) \\ F_{1s} = F(u_s+v_s)+F(u_s-v_s) \end{cases} \quad (16)$$

$$\begin{cases} E_{1c} = \frac{1}{j\pi v_c}\left[e^{\frac{j\pi(u_c-v_c)^2}{2}} - e^{\frac{j\pi(u_c+v_c)^2}{2}}\right] \\ E_{1s} = \frac{1}{j\pi v_s}\left[e^{\frac{j\pi(u_s-v_s)^2}{2}} - e^{\frac{j\pi(u_s+v_s)^2}{2}}\right] \end{cases} \quad (17)$$

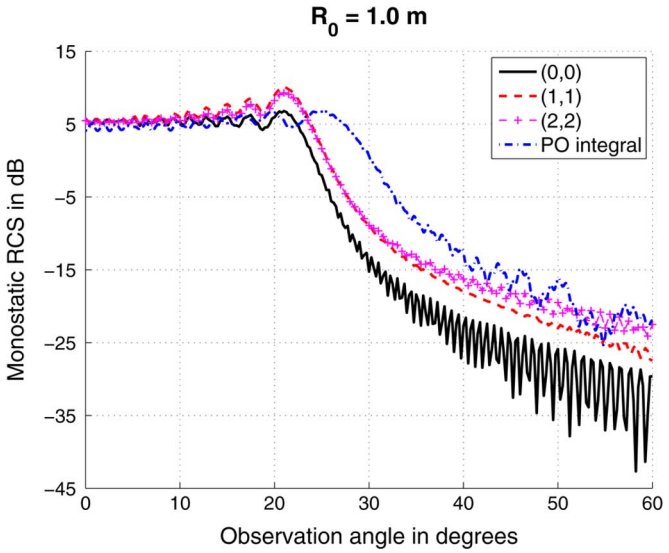

Fig. 2. Monostatic RCS versus the elevation angle θ_i for $a = b = 1$ m, $f = 15$ GHz ($\lambda = 2$ cm) and $\phi_i = \pi/2$ with $R_0 = 1$ m.

and

$$\begin{cases} u_c \pm v_c = \sqrt{\frac{R_0}{\lambda(1-c^2)}}\left[\frac{a(1-c^2)}{R_0} \pm 2c\right] \\ u_s \pm v_s = \sqrt{\frac{R_0}{\lambda(1-s^2)}}\left[\frac{b(1-s^2)}{R_0} \pm 2s\right] \end{cases}. \quad (18)$$

If $\theta_i = 0$, then $c = s = 0$ and $v_c = v_s = 0$. Thus, one has

$$\sigma_{\text{plate}}(0,\phi_i) = 4\pi R_0^2\left|F\left(\frac{a}{\sqrt{R_0\lambda}}\right)F\left(\frac{b}{\sqrt{R_0\lambda}}\right)\right|^2. \quad (19)$$

In addition, if $a \gg \sqrt{R_0\lambda}$ and $b \gg \sqrt{R_0\lambda}$, then $\lim_{\lambda\to 0}\sigma_{\text{plate}}(0,\phi_i) = \pi R_0^2$, since $|F(+\infty)| = 1/\sqrt{2}$. This corresponds to the RCS of a sphere of radius R_0 illuminated by a plane wave and derived in the far-field zone. We can interpret this result by considering the reciprocal problem: under the PO approximation, the field scattered by a plate which is illumintated by a *spherical* wave in the *near*-field zone is similar to that derived in the *far*-field zone by a sphere, which is illuminated by a *plane* wave, because in this case the sphericity of the wave is introduced via the object shape.

B. Numerical Results

In Fig. 2, the monostatic RCS of a square plate of dimensions $a = b = 1$ m is plotted versus the elevation angle θ_i for a frequency $f = 15$ GHz ($\lambda = 2$ cm) and for an azimuthal angle $\phi_i = \pi/2$. The distance $R_0 = 1$ m. In the legend, the label "(0,0)" means that the RCS is computed from (15), in which in (7), $(x = 0, y = 0)$, whereas for "(1,1)", $(x \neq 0, y \neq 0)$. They refer to the order of the terms in x and y retained in (7).

In addition, the label "PO integral" means that the RCS defined from (1) is computed from (2), for which, the double integral is computed numerically. In Fig. 3 the same variation as in Fig. 2 is plotted but with $R_0 = 5$ m. Since the PO approximation is used, the dimensions $a = 50\lambda$ and $b = 50\lambda$ must be large comparatively to the wavelength λ.

For $R_0 = 5$ m ($R_0 = 5a = 5b = 250\lambda$), a very good agreement is obtained between the different formulations. One can also notice that a Taylor series expansion of $(\hat{\mathbf{R}}\cdot\hat{\mathbf{n}})R_0^2/R^2$ over

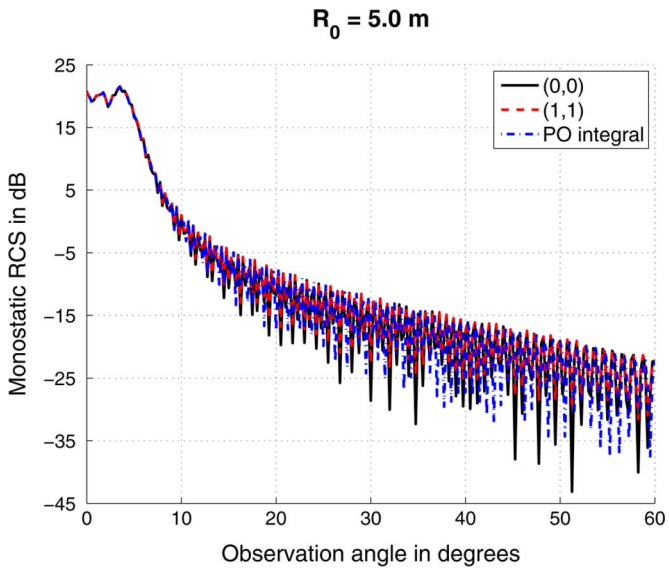

Fig. 3. Same configuration as in Fig. 2 but with $R_0 = 5$ m.

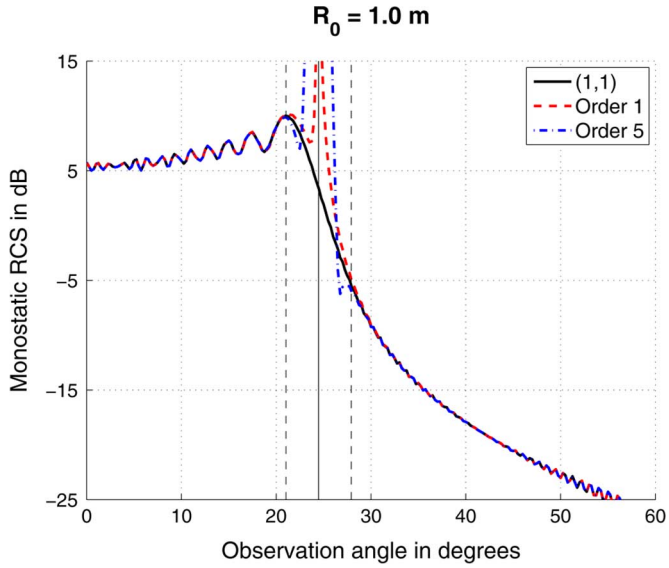

Fig. 4. Same configuration as in Fig. 3 but the Fresnel integral is computed from (20).

(x, y) up to the order zero is enough. However, in the phase term, it is necessary to make a Taylor series expansion over (x, y) up to the orders two.

For $R_0 = 1$ m ($R_0 = a = b = 50\lambda$), as the elevation angle increases, the difference between the "PO integral" and the "(1,1)" results increases, and the "(1,1)" results better match the "PO integral" ones than the "(0,0)" ones. From (12) and for $\theta_i = \pi/2$, one has $c = 0$ and $s = 1$, which implies that the ratio $\frac{s^2}{1-s^2} = \tan^2\theta_i$. That is why, from (15), that the contribution of "(1,1)" increases with θ_i. In addition, from (18), as v_s is an increasing function of $R_0, 1/v_s$ increases when R_0 decreases, and thus the E_{1s} contribution related to "(1,1)" increases when R_0 decreases.

As expected, the agreement with the "PO integral" is better in Fig. 3 than in Fig. 2, because the ratios a/R_0 and b/R_0 are smaller in Fig. 3. Indeed, the Taylor series expansions used in Section II are valid if the largest dimension of the object is much smaller than the distance R_0.

To obtain a better agreement with the "PO integral", in (7) it is possible to use a Taylor series expansion over (x, y) up to the order two, and to apply relations similar to (11), to derive analytically the integrations over x^2, y^2 and xy. Fig. 2 also presents the "(2,2)" results. As one can see, as θ_i increases, better agreement is obtained with the "PO integral" results. But the resulting formula becomes much more complicated.

Since one of the purposes of this paper is to obtain simple formulae of the RCS, Figs. 4 and 5 present the same variation as in Figs. 2 and 3, respectively, in which the Fresnel integral, $F(x)$, is expanded for $x \to \pm\infty$ as [7]

$$F(x) = \frac{1}{2}(1+j)\text{sign}(x) - e^{\frac{j\pi x^2}{2}} \times \left(\frac{j}{\pi x} + \frac{1}{\pi^2 x^3} - \frac{3j}{\pi^3 x^5}\right) + \mathcal{O}\left(\frac{1}{x^6}\right) \quad (20)$$

where $\text{sign}(x) = 1$ if $x \geq 0, -1$ otherwise.

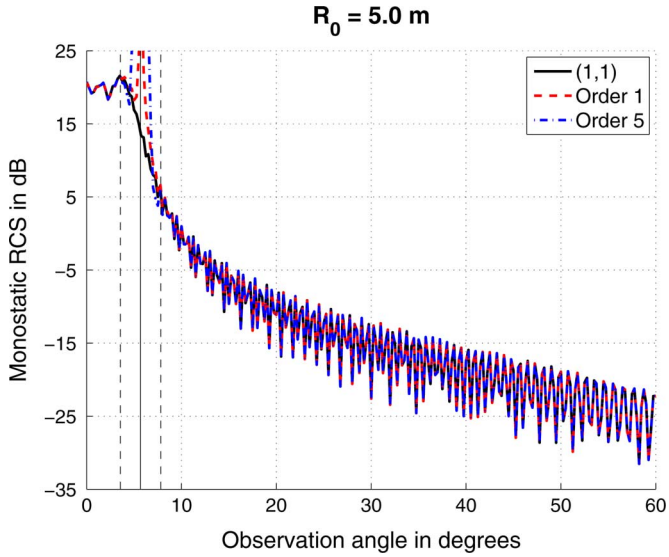

Fig. 5. Same configuration as in Fig. 3 but the Fresnel integral is computed from (20).

In Figs. 4 and 5, the label "Order n" means that in (20), the expansion is applied up to the order n, corresponding to the terms $1/x^p$ with $p = \{0, \ldots, n\}$.

For angles θ_i close to zero, a good agreement is observed between the different curves. For $R_0 = \{1, 5\}$ m, one has $a/\sqrt{R_0\lambda} = \{7.1, 3.2\} (a = b)$, which explains that when R_0 increases, the angular interval over θ_i, for which (20) is not satisfied, is shifted toward the smaller angles θ_i. Furthermore, since $u_s \pm v_s = \sqrt{R_0/\lambda}[(b/R_0)\cos\theta_i \pm 2\tan\theta_i]$, for

$$\theta_i = \theta_{i0} = \arcsin\left(-\frac{R_0}{b} + \sqrt{1 + \frac{R_0^2}{b^2}}\right) \quad (21)$$

the argument of the Fresnel integral $u_s - v_s$ vanishes, and thus (20) cannot be applied. For $R_0 = \{1, 5\}$ m, $\theta_{i0} = \{24.5, 5.7\}^\circ$,

which explains in Figs. 4 and 5 around θ_{i0} the non-physical enhancement of the RCS up to the orders 1 and 5. The vertical solid-line indicates the value of θ_{i0}. One also observes that the higher-order terms do not improve the agreement with the "PO integral" results.

In (20), if only the terms up to $1/x$ orders are retained, then for $|x| \geq 1.2 = x_0$ the relative error between (20) and (14) is smaller than 0.05. Thus, it is possible to derive a range $\theta_i \in [\theta_{i0} - \Delta\theta_i; \theta_{i0} + \Delta\theta_i]$ corresponding to $|u_s \pm v_s| \leq x_0$, for which (20) is not satisfied. It can be shown that

$$\Delta\theta_i \approx \frac{x_0}{2}\sqrt{\frac{\lambda R_0}{R_0^2 + b^2}}. \tag{22}$$

The lower limit, $\theta_{i0} - \Delta\theta_i$, and the upper limit $\theta_{i0} + \Delta\theta_i$, are shown in Figs. 4 and 5 with vertical dashed lines. For $R_0 = \{1, 5\}$ m, $\Delta\theta_i = \{3.5, 2.2\}^{\circ}$ and the difference between the results obtained from (20) and (14) does not exceed $\{0.15, 0.63\}$ dB for $\theta_i \notin [\theta_{i0} - \Delta\theta_i; \theta_{i0} + \Delta\theta_i]$.

Then, substituting (20) (by keeping only the first two terms) into (19), one has

$$\begin{aligned}\sigma_{\text{plate}}(0, \phi_i) &\approx \pi R_0^2 \left| e^{\frac{j\pi}{4}} - \frac{j e^{jX_a^2}}{X_a\sqrt{\pi}} \right|^2 \left| e^{\frac{j\pi}{4}} - \frac{j e^{jX_b^2}}{X_b\sqrt{\pi}} \right|^2 \\ &\approx \pi R_0^2 \left[1 + \frac{1}{\pi X_a^2} + \frac{2\cos\left(X_a^2 - \frac{3\pi}{4}\right)}{X_a\sqrt{\pi}} \right] \\ &\quad \times \left[1 + \frac{1}{\pi X_b^2} + \frac{2\cos\left(X_b^2 - \frac{3\pi}{4}\right)}{X_b\sqrt{\pi}} \right] \end{aligned} \tag{23}$$

with

$$\begin{aligned} X_a &= a\sqrt{\frac{\pi}{2\lambda R_0}} \\ X_b &= b\sqrt{\frac{\pi}{2\lambda R_0}}. \end{aligned} \tag{24}$$

Equation (23) is valid for $\theta_i = 0$ and for X_a and X_b larger than $\sqrt{\pi/2}x_0 \approx 1.51$, and shows in the near-field zone that the monostatic RCS has a pseudo-periodical behavior with respect to the distance R_0 and the wavelength λ.

This study was led for an azimuthal angle $\phi_i = \pi/2$. For any ϕ_i, it is easy to obtain formulae similar to (21) and (20), and to define the validity domain of (20).

IV. Case of a Disk

A. Derivation of the RCS

In polar coordinates $\{x = r\cos\phi, y = r\cos\phi\}$ with $\{\phi \in [0; 2\pi], r \in [0; a]\}$, in which a is the disk radius, (6) and (7) become

$$\begin{aligned} R &\approx R_0 - r\sin\theta_i\cos(\phi - \phi_i) + \frac{r^2}{2R_0}\left(1 - \frac{\sin^2\theta_i}{2}\right) \\ &\quad - \frac{r^2\sin^2\theta_i}{4R_0}\cos(2[\phi - \phi_i]) \end{aligned} \tag{25}$$

and

$$(\hat{\mathbf{R}}\cdot\hat{\mathbf{n}})\frac{R_0^2}{R^2} \approx \cos\theta_i\left[1 + \frac{3r\sin\theta_i\cos(\phi - \phi_i)}{R_0}\right]. \tag{26}$$

Reporting (25) and (26) into (1) and (2), using the variable transformation $\eta = r/a$ and performing the integration over ϕ, it can be shown with $dS = dxdy = rdrd\phi = a^2\eta d\eta d\phi$ that

$$\begin{aligned}\sigma_{\text{disk}}(\theta_i) = \frac{16\pi^3 a^4\cos^2\theta_i}{\lambda^2} \Bigg| \int_0^1 e^{j\eta^2u^2\left(\frac{2}{\sin^2\theta_i} - 1\right)} \\ \times \left[f_0(4v\eta u, \eta^2u^2) \right. \\ \left. + \frac{3j\eta u}{v} f_1(4v\eta u, \eta^2u^2) \right] \eta d\eta \Bigg|^2 \end{aligned} \tag{27}$$

where $\{f_1, f_0\}$ are expressed from (A4) and (A6), and u and v are given by

$$u = \frac{a\sin\theta_i\sqrt{\pi}}{\sqrt{\lambda R_0}} \quad v = \sqrt{\frac{\pi R_0}{\lambda}}. \tag{28}$$

For $\theta_i = 0, u = 0$ and from (A4) and (A6), $f_0(0, 0) = 1$ and $f_1(0, 0) = 0$ since $J_n(0) = 0$ if $n \geq 1, 1$ otherwise $(n = 0)$. Thus, (27) becomes

$$\begin{aligned}\sigma_{\text{disk}}(0) &= \frac{16\pi^3 a^4\cos^2\theta_i}{\lambda^2} \left| \int_0^1 \eta e^{\frac{2j\pi a^2\eta^2}{\lambda R_0}} d\eta \right|^2 \\ &= 2\pi R_0^2 \left[1 - \cos\left(\frac{2\pi a^2}{\lambda R_0}\right) \right]. \end{aligned} \tag{29}$$

Equation (23) shows that the monostatic RCS has a periodical behavior with respect to the distance R_0 and to the wavelength λ.

B. Study of the Functions f_0 and f_1

From (A4) and (A6), the functions f_0 and f_1 are expressed from a summation over m, with $m \in [0; \infty[$. Thus, to compute this sum, it is necessary to truncate it at the order $m = M$. For the simulations, the frequency $f = 10$ GHz ($\lambda = 3$ cm) and the radius $a = 0.3$ m $= 10\lambda$. In the integral of (27), the functions f_0 and f_1 depend on ηu and v. Since $\sin\theta_i \in [0; 1] (\theta_i \geq 0)$ and $\eta \in [0; 1], \eta u = \eta_u \in [0; u_{\max}]$ with $u_{\max} = u/\sin\theta_i$.

In Fig. 6, for $R_0 = 1$ m, the moduli of the sums over M of the functions f_0 (top) and $3\eta_u f_1/v$ (bottom) are plotted versus the parameter $\eta u = \eta_u$. As one can see, the plots show discrepancies between different partial sums for the larger values of η_u, and the partial sums are decreasing functions of η_u. Indeed, for the smaller values of η_u (smaller than 1), only the zero-order term $(M = m = 0)$ contributes, which means that $f_0(\alpha, \beta) \approx J_0(\alpha)J_0(\beta)$ and $f_1(\alpha, \beta) \approx -J_1(\alpha)J_0(\beta)$. For $\eta_u = 0, \alpha = \beta = 0$ and $f_0(\alpha, \beta) = 1$, whereas $f_1(\alpha, \beta) = 0$.

In Fig. 6, the functions $|f_0(\alpha, \beta)| = |J_0(\alpha)|$ and $3\eta_u|J_1(\alpha)/v|$ (which is similar to taking $\beta = 0$) are also plotted. As one can see, the comparisons show that the impact on β is minor, because the curves with the label "$J_0(\alpha)$" are close to that with the label "$M = 2$". We can conclude that $J_0(\beta) \approx 1$ for $\eta \in [0; 1]$.

For $R_0 = 5$ m, simulations (which are not reported in this paper) show that the contributions of $3\eta_u|f_1|/v$ and of the higher order terms in the sums $(m > 0)$ are smaller than the

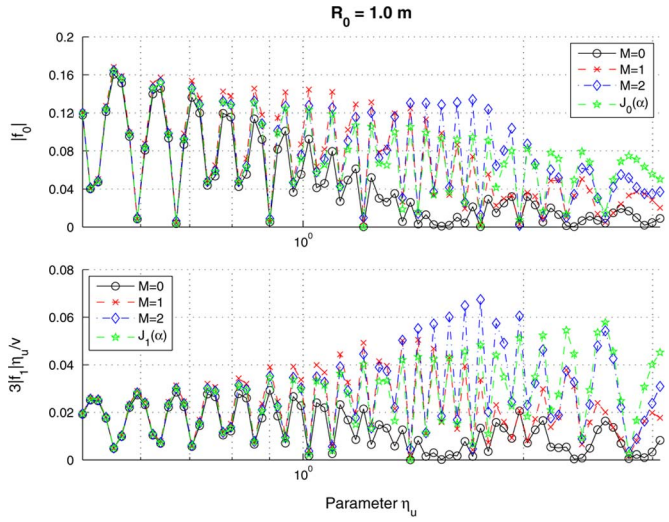

Fig. 6. Moduli of the sums over M of the functions f_0 (top) and $3\eta_u f_1/v$ (bottom) versus the parameter $\eta u = \eta_u$ for $R_0 = 1$ m.

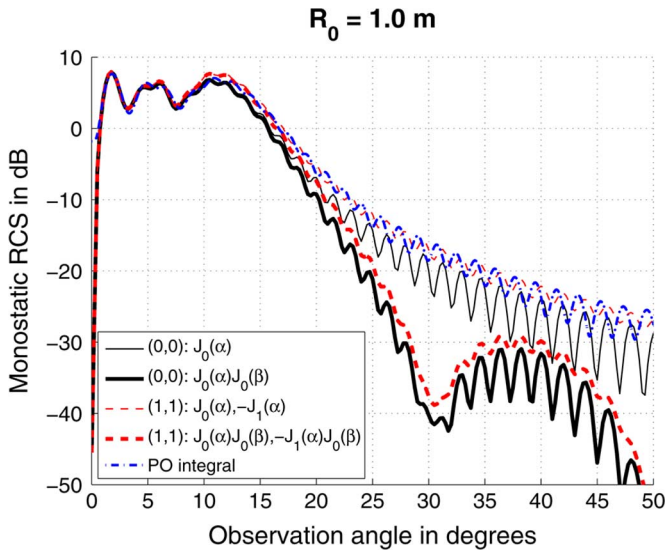

Fig. 7. Monostatic RCS versus the observation angle θ_i for $a = 0.3$ m, $f = 10$ GHz ($\lambda = 3$ cm) and $R_0 = 1$ m.

ones obtained for $R_0 = 1$ m. Indeed, for $R_0 = \{1, 5\}$ m, $u_{\max} = \{3.07, 1.37\}$ and $v = \{10.23, 22.88\}$.

C. Numerical Results of the RCS

In Fig. 7, the monostatic RCS is plotted versus the observation angle θ_i for a radius $a = 0.3$ m, a frequency $f = 10$ GHz ($\lambda = 3$ cm) and a distance $R_0 = 1\text{m} = 33.3\lambda$. In Fig. 8, the same configuration is plotted, but for $R_0 = 5\text{m} = 166.6\lambda$.

In the legend, the labels "(0,0)", "(1,1)" and "PO Integral" are the same as in Figs. 2–3. More precisely, in polar coordinates, label "(0,0)" means that the RCS is computed from (27), in which in (26), $r = 0$, whereas for "(1,1)", $r \neq 0$. In addition, for the labels "(0,0)" and "(1,1)" the expressions of the functions $\{f_0(\alpha, \beta), f_1(\alpha, \beta)\}$ are given, respectively. They are computed from (A4) and (A6), in which the sums are truncated at the order zero ($m = 0$).

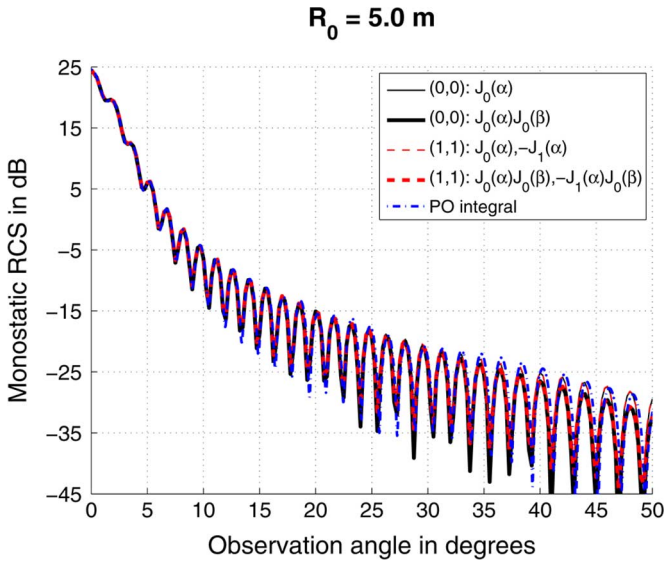

Fig. 8. Same configuration as in Fig. 7, but for $R_0 = 5$ m.

For $R_0 = 1$ m and when $\beta = 0$ in the expressions of f_0 and f_1, a better agreement is obtained with the "PO Integral" results. It is consistent with the observations made in Fig. 6. In addition, the "(1,1)" results are similar to "(0,0)" results with smaller local variations. Comparing with the results of Fig. 2 (case of a rectangular plate of dimensions $a = b = 50\lambda$ with $R_0 = 50\lambda$), in (7) the effects of the terms over x and y are less important for a disk of diameter $2a = 20\lambda$ with $R_0 = 33.3\lambda$. For $R_0 = 5$ m, all formulations give similar results and a very good agreement is found with the "PO integral" results.

As a conclusion, from (27) and (28) with $f_0(\alpha, \beta) \approx J_0(\alpha)$ and $f_1(\alpha, \beta) \approx -J_1(\alpha)$, the monostatic RCS of a disk can be simplified as

$$\sigma_{\text{disk}}(\theta_i) \approx \frac{16\pi^3 a^4 \cos^2\theta_i}{\lambda^2} \left| \int_0^1 e^{\frac{2\pi j\eta^2 a^2}{\lambda R_0}\left(1-\frac{\sin^2\theta_i}{2}\right)} \times \left[J_0\left(\frac{4\pi\eta a \sin\theta_i}{\lambda}\right) - \frac{3j\eta a \sin\theta_i}{R_0} J_1\left(\frac{4\pi\eta a \sin\theta_i}{\lambda}\right)\right] \eta d\eta \right|^2. \quad (30)$$

The difficulty is to find a way to analytically derive the integration over η. In optics domain, this type of integral is involved in the problem of diffraction of converging spherical waves by circular apertures (see for example [8, Ch. 8, Sec. 8]). First, the exponential term is expanded as

$$e^{\frac{2\pi j\eta^2 a^2}{\lambda R_0}\left(1-\frac{\sin^2\theta_i}{2}\right)} = \sum_{n=0}^{n=\infty} \frac{1}{n!}\left[\frac{2\pi j\eta^2 a^2}{\lambda R_0}\left(1-\frac{\sin^2\theta_i}{2}\right)\right]^n. \quad (31)$$

Then, substituting (31) into (30), the integral can be derived in terms of Lommel's functions, which are expressed from an infinite series of Bessel functions. These functions are not easy to compute numerically. More recently, Qing Cao [9] has derived

an integral similar to (30) in an elegant manner by introducing the Jinc_n function, which is

$$\mathrm{Jinc}_n(u) = \frac{1}{u^{2n+2}}\int_0^u v^{2n+1}J_0(v)dv = n!\sum_{m=0}^{m=n}\frac{(-2)^m}{(n-m)!}\frac{J_{m+1}(u)}{u^{m+1}}. \quad (32)$$

For example, one has

$$\begin{cases} \mathrm{Jinc}_0(u) = \frac{J_1(u)}{u} \\ \mathrm{Jinc}_1(u) = \frac{J_1(u)}{u} - \frac{2J_2(u)}{u^2} \\ \mathrm{Jinc}_2(u) = \frac{J_1(u)}{u} - \frac{4J_2(u)}{u^2} + \frac{8J_3(u)}{u^3} \\ \mathrm{Jinc}_3(u) = \frac{J_1(u)}{u} - \frac{6J_2(u)}{u^2} + \frac{24J_3(u)}{u^3} - \frac{44J_4(u)}{u^4} \end{cases}. \quad (33)$$

Thus, from (32) and using an integration by parts, it can be shown that

$$\mathrm{Jinc}_n^{(1)}(u) = \frac{1}{u^{2n+3}}\int_0^u v^{2n+2}J_1(v)dv = \frac{1}{u}[2(n+1)\mathrm{Jinc}_n(u) - J_0(u)]. \quad (34)$$

On a numerical point of view, formulae (32) and (34) are very useful, because the computation of the Bessel function J_{m+1} for $m > 1$ is obtained from J_m and J_{m-1} by using the relation $J_{m+1}(u) = [(2m)/u]J_m(u) - J_{m-1}(u)$. Thus, only J_0 and J_1 are necessary.

The Substitution of (34), (32) and (31) into (30) and the calculation of the integration over η yield

$$\sigma_{\mathrm{disk}}(\theta_i) \approx \frac{16\pi^3 a^4\cos^2\theta_i}{\lambda^2}\left|\sum_{n=0}^{n=\infty}\frac{\gamma^n}{n!} \times \left[\mathrm{Jinc}_n(\alpha) - \frac{3ja\sin\theta_i}{R_0}\mathrm{Jinc}_n^{(1)}(\alpha)\right]\right|^2 \quad (35)$$

with

$$\alpha = \frac{4\pi a\sin\theta_i}{\lambda} \quad \gamma = \frac{2\pi j a^2}{\lambda R_0}\left(1 - \frac{\sin^2\theta_i}{2}\right). \quad (36)$$

If $\theta_i = 0$, then $\alpha = 0$ and since $\mathrm{Jinc}_n(0) = 1/[2(n+1)]$, (35) is found. In addition, Cao [9] showed that the sum over n of (35) can be truncated at the order $n = N$ with a relative error ϵ_0 if

$$\frac{(\pi\delta_0)^{2N}}{(2N+1)(N!)^2} \le \epsilon_0 \quad \delta_0 = \frac{2a^2}{\lambda R_0}(1 - \frac{\sin^2\theta_i}{2}). \quad (37)$$

Taking a relative error of 0.05 as for the rectangular plate, from (37), N can be computed, and thus the sum over n of (35) is reduced to $n \in [0; N]$.

In Fig. 9, N is plotted versus δ_0 for $\epsilon_0 = 0.05$. In addition, the values obtained from a linear regression, $N = -1.00 + 8.20\delta_0$, are represented. For example, with the parameters of Figs. 7 and 8, if $\theta_i = 0$ (giving the upper value of N), for $R_0 = \{1, 5\}$ m, $\delta_0 = \{6, 1.2\}$, leading to $N = \{48, 8\}$. Thus, as R_0 decreases, the number of terms increases. On the contrary, as θ_i increases, the number of terms decreases since δ_0 is a decreasing function of θ_i.

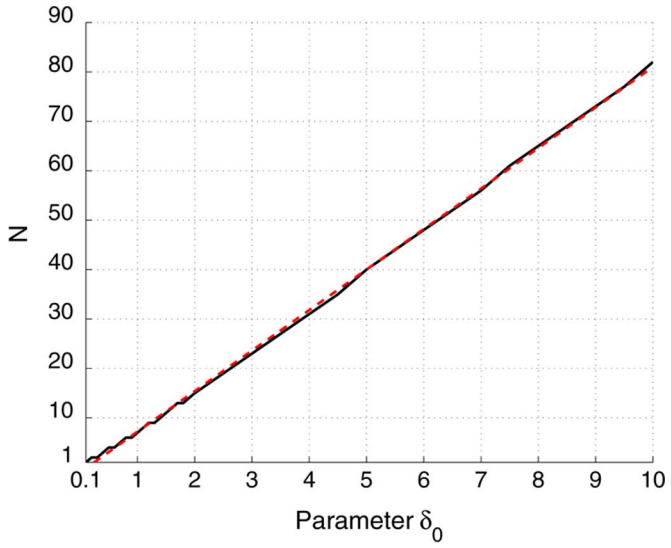

Fig. 9. N versus δ_0 for $\epsilon_0 = 0.05$. In addition, the values obtained from a linear regression are plotted.

Figs. 10 and 11 compare (30) with the series (35) truncated at the order N. As one can see, the last order N is enough to approximate series (35) and as θ_i increases, the order N decreases. For $R_0 = \{1, 5\}$ m, $N = \{48, 8\}$ and then the difference between the results computed from (30) and (35) does not exceed $\{0.9, 0.2\}$ dB. In fact, this difference decreases as the observation angle increases. Furthermore, in Fig. 10, for $\theta_i = 35^\circ, \delta_0 = 5.01$, which leads from the chart of Fig. 9 to $N = 40$. This value is consistent with the observations. When $N = 0, \mathrm{Jinc}_0(u) = J_1(u)/u$, which corresponds to the diffraction by a circular aperture in the far-field zone.

V. Far-Field Criterion

From the closed-from expressions obtained in the preceding sections, this section presents a criterion of the far-field condition which separates the Fresnel and Fraunhofer zones defined from the well-known criterion $R_0/\lambda \ge (2D^2)/\lambda^2$, in which D is the "characteristic dimension" of the object. For practical needs, it is more convenient to use the formulae established in the far-field zone, because they are often more compact than the ones obtained in the near-field zone. Thus, it is interesting to know when the RCS derived under the far-field assumption can be applied.

To study D with respect to the incidence angle and the object shape, let us define $D = \sqrt{\nu}D_{\max}$, in which $D_{\max}$ is the largest dimension of the object. For a rectangular plate of dimensions a and b, $D_{\max} = \sqrt{a^2 + b^2}$, and for a disk of radius a, $D_{\max} = 2a$.

At the top of Fig. 12, the monostatic RCS of a square plate [see (19)] of dimensions $a = b = 0.5$ m is plotted versus the normalized distance R_0/λ for $\theta_i = \{0, 30\}^\circ$ and $\phi_i = 0^\circ$. At the bottom, the same configuration [see (29)] is plotted for a disk of same area S (radius $a = 0.5/\sqrt{\pi}$ m). In addition, in Fig. 12, the monostatic RCS (horizontal line) obtained for $R_0 \to \infty, \sigma^\infty$, is plotted. For $\theta_i = 0^\circ, \sigma^\infty = (4\pi S^2)/\lambda^2$. The vertical lines give the values of $R_0/\lambda = R_0^\infty/\lambda$ when the

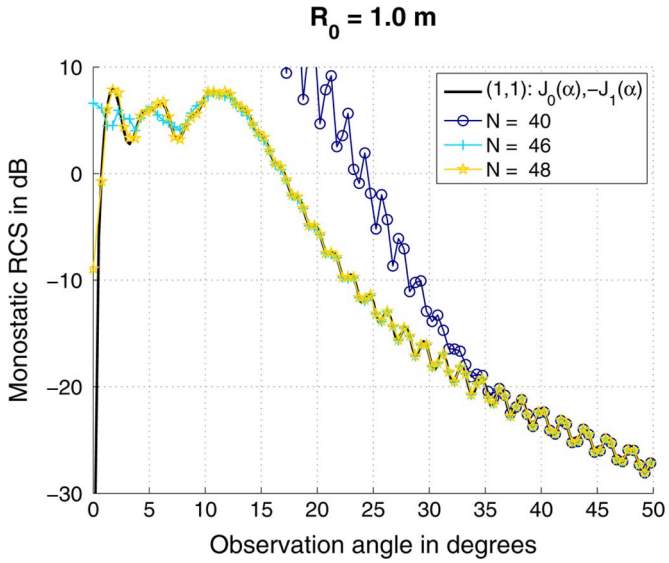

Fig. 10. Same configuration as in Fig. 7.

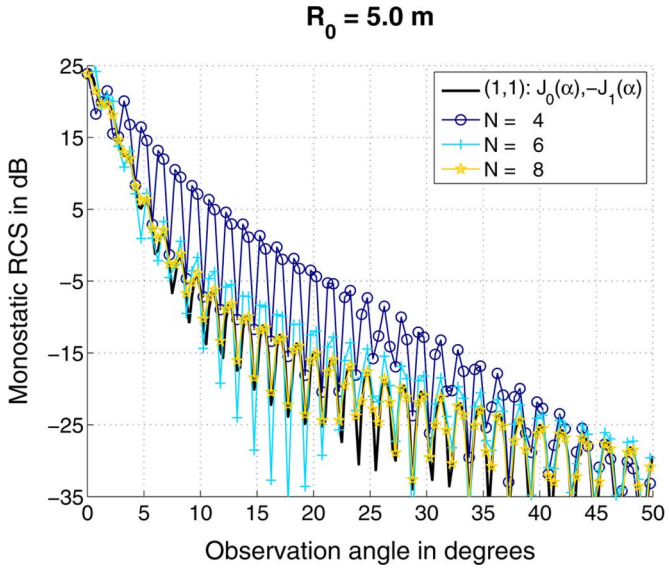

Fig. 11. Same configuration as in Fig. 8.

difference between the monostatic RCS and its asymptotic value σ^{∞} reaches 1 dB.

The values $R_0^{\infty}/\lambda, R_0^{\infty}$, and ν are collected in Table I for a square plate $(D_{\max} = \sqrt{2}a)$ and for a disk $(D_{\max} = 2a)$ with $\theta_i = \{0, 30\}^{\circ}$. One can then observe that ν depends on the object shape and on the observation angle.

For an infinite distance R_0 and for $\theta_i = 0^{\circ}$, the monostatic RCS are obtained from (19) and (29), in which the arguments of the functions are close to zero. A means to derive ν is to expand these functions around zero. Thus, since $F(x) = x + (j\pi x^3)/6 - (\pi^2 x^5)/40 + \mathcal{O}(x^7)$ and $\cos(x) = 1 - x^2/2 + x^4/24 + \mathcal{O}(x^6)$, one has for $\theta_i = 0$

$$\begin{cases} \sigma_{\text{plate}}(0,\phi_i) \approx \sigma^{\infty}\left(1 - \frac{\pi^2(a^4+b^4)}{45(R_0\lambda)^2}\right) \\ \sigma_{\text{disk}}(0) \approx \sigma^{\infty}\left(1 - \frac{\pi^2 a^4}{3(R_0\lambda)^2}\right) \end{cases}. \quad (38)$$

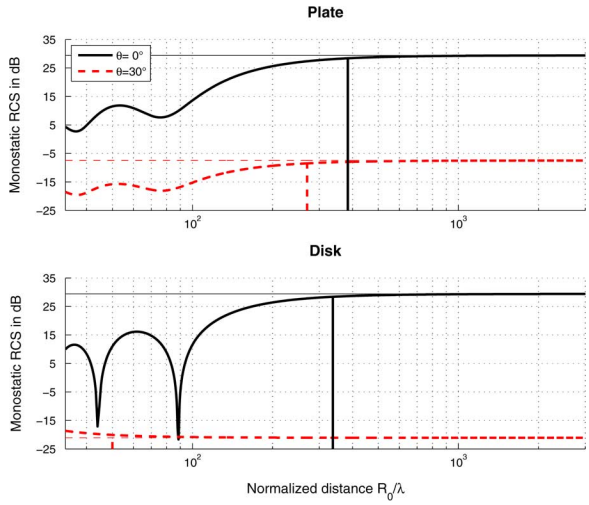

Fig. 12. Monostatic RCS of a square plate $a = b = 0.5$ m (top) and a disk $a = 0.5/\sqrt{\pi}$ (bottom) versus the normalized distance R_0/λ and for $\theta_i = \{0, 30\}^{\circ}$. The frequency $f = 10$ GHz ($\lambda = 3$ cm).

TABLE I
VALUES RELATED TO THE FAR-FIELD CRITERION

	Square Plate ($D_{\max} = \sqrt{2}a$)		Disk ($D_{\max} = 2a$)	
	$\theta_i = 0^{\circ}$	$\theta_i = 30^{\circ}$	$\theta_i = 0^{\circ}$	$\theta_i = 30^{\circ}$
R_0^{∞}/λ	382.3	270.0	336.7	50.0
R_0^{∞} (m)	11.5	8.1	10.1	1.5
$\nu = \frac{\lambda R_0^{\infty}}{2D_{\max}^2}$	0.345	0.243	0.303	0.045

The far field distance R_0^{∞} can then be derived when the ratio $(\sigma_{\text{plate,disk}})/(\sigma^{\infty})$ is greater than a threshold $s_0 \in]0;1[$ defined as $\sigma_{\text{plate,disk}} = s_0\sigma^{\infty}$. Therefore, from (38), it can be shown that

$$\begin{cases} \frac{R_0^{\infty}}{\lambda} = \frac{2D_{\max}^2}{\lambda^2}\frac{\pi}{\sqrt{90(1-s_0)}}\sqrt{\frac{a^4+b^4}{2(a^2+b^2)^2}} & \text{(Plate)} \\ \frac{R_0^{\infty}}{\lambda} = \frac{2D_{\max}^2}{\lambda^2}\frac{\pi}{8\sqrt{3(1-s_0)}} & \text{(Disk)} \end{cases}. \quad (39)$$

Since $\nu = (\lambda R_0^{\infty})/(2D_{\max}^2)$, the term after the ratio $(2D_{\max}^2)/\lambda^2$ is equal to ν. Thus, taking a difference of 1 dB $(s_0 = 0.794)$ between σ^{∞} and $\sigma_{\text{plate,disk}}$, the formulae lead to $\nu = \{0.365, 0.301\}$, which is consistent with the values given in Table I for $\theta_i = 0^{\circ}$. For a square plate $(a = b)$ and for a disk, (39) show that ν is independent of λ and of the dimensions of the object. Simulations, not reported in the paper, confirm this remark.

For $\theta_i > 0^{\circ}$ it is more difficult to obtain closed-form expressions of the limit distance R_0^{∞}. Thus, in this paper only simulations with respect to θ_i are presented. At the top of Fig. 13, the normalized parameter $\nu/\nu_{\theta_i=0}$ is plotted versus the observation angle θ_i with the same parameters as in Fig. 12. At the bottom, the absolute difference $|\sigma_{R_0=1\text{m}} - \sigma_{R_0=R_0^{\infty}}|$ is plotted versus the incidence angle θ_i. As one can show, for a square plate, ν is not very sensitive to the observation angle and $\nu/\nu_{\theta_i=0} \approx 0.786$, which means that the limit distance R_0^{∞} is a decreasing function of the observation angle. In addition, as the observation angle increases, the RCS absolute difference (bottom) slightly increases.

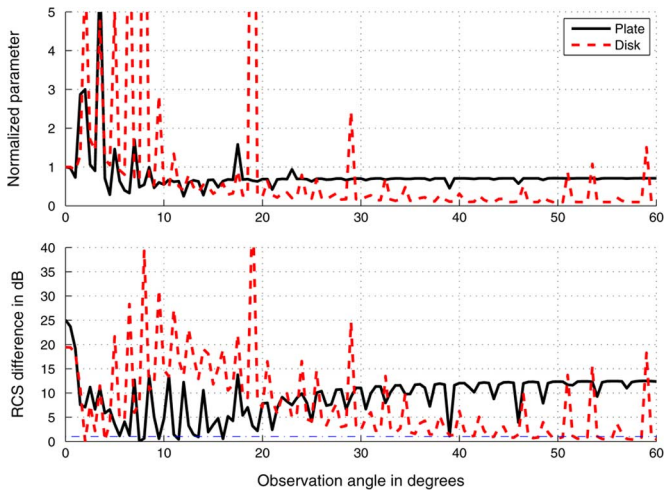

Fig. 13. At the top, normalized parameter $\nu/\nu_{\theta_i=0}$ versus the observation angle θ_i with the same parameters as in Fig. 12. At the bottom, the absolute difference $|\sigma_{R_0=1\mathrm{m}} - \sigma_{R_0=R_0^\infty}|$ versus the incidence angle θ_i.

For a disk, the behaviors are different. Indeed, the final value obtained for $\nu/\nu_{\theta_i=0} \approx 0.1$ is approximately 8 times smaller than that obtained for a square plate of same area. This implies that the limit distance R_0^∞ is smaller than that obtained for a square plate. Furthermore, the RCS absolute difference decreases faster than that of the square plate.

VI. Conclusion

In this paper, the monostatic RCS of a plate and a disk were derived in near-field zone under the physical optics (PO) approximation and for oblique incidence angles (or observation angles). The PO approximation requires the computation of a double numerical integration. To avoid this integration and to predict the behavior of the RCS in near zone, useful formulae were derived.

For a rectangular plate, the monostatic RCS is expressed in terms of Fresnel integrals. In addition, to avoid the calculation of these functions, an approximation was proposed, which allows one to obtain a simple expression of the RCS. A validity domain of this approximation was also presented.

For the case of a disk, the monostatic RCS is expressed in terms of infinite series of the Jinc_n and $\mathrm{Jinc}_n^{(1)}$ special functions, which depend on Bessel functions of the first kind. To obtain numerical results, the series must be truncated. The results showed that the number of the terms retained in the series, which is obtained easily from a chart, decreases as the observation angle θ_i and the distance R_0 increase.

Last, the far-field condition was investigated from the well-known criterion $R_0/\lambda \geq (2D^2)/\lambda^2 = \nu(2D_{\max}^2)/\lambda^2$, in which $D_{\max}$ is the largest dimension of the object, and ν was derived from closed-from expressions at normal incidence. The simulations showed for a square plate and a disk of same area that ν is of the order of 0.35 and 0.30, respectively, and that these values are independent of the dimensions of the objects. In addition, as the observation angle increases, the limit far-field distance decreases and it is smaller for the disk.

Appendix A

The following integral over ϕ must be derived

$$f_0(\alpha,\beta) = \frac{1}{2\pi}\int_0^{2\pi} e^{-j\alpha\cos(\phi-\phi_i)-j\beta\cos(2[\phi-\phi_i])}d\phi. \quad \text{(A1)}$$

The complex exponential can be expressed as [7]

$$\begin{cases} e^{-j\alpha\cos(\phi-\phi_i)} = \sum_{n=-\infty}^{n=+\infty} j^n J_n(-\alpha)e^{jn(\phi-\phi_i)} \\ e^{-j\beta\cos(2[\phi-\phi_i])} = \sum_{m=-\infty}^{m=+\infty} j^m J_m(-\beta)e^{2jm(\phi-\phi_i)} \end{cases} \quad \text{(A2)}$$

where J_m is the Bessel function of the first kind and of order m. Substituting (A2) into (A1) and performing the integration over ϕ, it can be shown that

$$f_0(\alpha,\beta) = \sum_{n,m} j^{n+m} J_n(-\alpha)J_m(-\beta)e^{-j\phi_i(n+2m)}\delta_{0,n+2m} \quad \text{(A3)}$$

where $\delta_{i,j}$ is the Kronecker symbol defined as $\delta_{i,j} = 1$ if $i = j, 0$ otherwise. The use of the following relations, $J_m(-x) = (-1)^m J_m(x)$ and $J_{-2m}(x) = (-1)^{2m}J_{2m}(x) = J_{2m}(x)$, leads then to

$$\begin{aligned} f_0(\alpha,\beta) &= \sum_{m=-\infty}^{m=+\infty} j^m J_{2m}(\alpha)J_m(\beta) \\ &= J_0(\alpha)J_0(\beta) + 2\sum_{m=1}^{m=+\infty} j^m J_{2m}(\alpha)J_m(\beta). \end{aligned} \quad \text{(A4)}$$

In addition, since

$$\begin{aligned} f_1(\alpha,\beta) &= \frac{-j}{2\pi}\int_0^{2\pi} \cos(\phi-\phi_i)e^{-j\alpha\cos(\phi-\phi_i)-j\beta\cos(2[\phi-\phi_i])}d\phi \\ &= \frac{\partial f_0(\alpha,\beta)}{\partial\alpha} \end{aligned} \quad \text{(A5)}$$

from (A4), the resulting equation is

$$\begin{aligned} f_1(\alpha,\beta) = -J_1(\alpha)J_0(\beta) + \sum_{m=1}^{m=+\infty} j^m \\ \times J_m(\beta)[J_{2m-1}(\alpha) - J_{2m+1}(\alpha)]. \end{aligned} \quad \text{(A6)}$$

Acknowledgment

The authors would like thank the anonymous reviewers for their useful comments and suggestions and Dr. N. Pinel for his comments.

References

[1] M. H. Vogel, "The Physical Optics Approximation in the Near-Field Region," TNO Physics and Electronics Laboratory, Rep. no. FEL 1989-100n, Mar. 1989.

[2] S. R. Legault and A. Louie, "Validation and implementation of a near-field Physical Optics formulation," Technical Memorandum, DRDC Ottawa TM 2004-131, Aug. 2004, pp. 56–.
[3] C. L. YU, R. Kipp, D. J. Andersh, and S. W. Lee, "Near-field electromagnetic modeling and analysis," presented at the IEEE AP-S Int. Symp. and URSI Radio Science Meeting, Montreal, Canada, Jul. 13–18, 1997.
[4] S. W. Lee and S. K. Jeng, "NcPTD 1.2 A High Frequency Near-Field RCS Computation Code Based on Physical Theory of Diffraction," DEMACO, Inc., Champaign, IL, Jun. 1991.
[5] J. M. Taylor and A. J. Terzuoli, "On the Concept of near field radar cross section," presented at the IEEE AP-S Int. Symp. and URSI Radio Science Meeting, Montreal, Canada, Jul. 13–18, 1997.
[6] P. Pouliguen, P. Gadenne, and J. Y. Marty, "Radar reflectivity of a target illuminated by a spherical wave," presented at the AGARD Conf. Radar Signature Analysis and Imaging of Military Targets, Ankara, Turkey, Oct. 7–10, 1996.
[7] M. Abromowitz and I. A. Stegun, *Handbook of Mathematical Functions*. New York: Dover, 1972.
[8] M. Born and E. Wolf, *Principle of Optics*, 6th ed. New York: Pergamon Press, 1989.
[9] Q. Cao, "Generalized Jinc functions and their application to focusing and diffraction of circular apertures," *J. Opt. Soc. Am. A*, vol. 20, no. 4, pp. 661–667, 2003.
[10] A. Michaeli, "Elimination of infinities in equivalent edge currents, Part I: Fringe current components," *IEEE Trans. Antennas. Propag.*, vol. 34, no. 7, pp. 661–667, 1986.
[11] A. Michaeli, "Elimination of infinities in equivalent edge currents—Part II: Physical optics components," *IEEE Trans. Antennas. Propag.*, vol. 34, no. 8, pp. 1034–1037, 1986.
[12] P. Pouliguen, R. Hémon, J. F. Damiens, and J. Saillard, "Analytical formulas for radar cross section of flat plates in near field and normal incidence," *Progress In Electromagn. Res. B*, vol. 8, pp. 263–279, 2008.

Christophe Bourlier (M'99) was born in La Flèche, France, on July 6, 1971. He received the M.S. degree in electronics and the Ph.D. degree from the University of Rennes, Rennes, France, in 1995 and 1999, respectively.

While at the University of Rennes, he was with the Laboratory of Radiocommunication where he worked on antennas coupling in the VHF-HF band. Now, he is a member of the Radar Team, Institut de Recherche en Electrotechnique et Electronique de Nantes Atlantique (IREENA) Laboratory, France, Polytech'Nantes, University of Nantes, France. He is an Assistant Researcher at the National Center for Scientific Research where he works on electromagnetic wave scattering from rough surfaces and objects for remote sensing applications. He is author of more than 90 journal articles and conference papers.

Philippe Pouliguen was born in Rennes, France, in 1963. He received the Ph.D. degree from the University of Rennes 1, Rennes, France, in 1990.

In 1990, he joined the Délégation Générale de l'Armement (DGA), Centre d'Electronique de l'Armement (CELAR), Bruz, France. He is currently working as a "DGA expert" in electromagnetic radiation and radar signatures analysis. He is also in charge of the Expertise and ElectoMagnetism Computation (EMC) Laboratory, CELAR. His research interests include electromagnetic scattering and diffraction, radar cross section (RCS) measurement and modeling, high frequency methods, radar signal processing and analysis, antenna scattering problems and electronic band gap materials. These activities are done in close collaboration with French Universities. In these fields, he has published more than 25 articles in refereed journals and more than 70 conference papers.